JACS
JOURNAL OF THE AMERICAN CHEMICAL SOCIETY

Article

pubs.acs.org/JACS

Improving the Charge Transport in Self-Assembled Monolayer Field-Effect Transistors: From Theory to Devices

Christof M. Jäger,[†] Thomas Schmaltz,[§] Michael Novak,[§] Artoem Khassanov,[§] Alexei Vorobiev,[∥] Matthias Hennemann,[†] Andreas Krause,[†] Hanno Dietrich,[‡] Dirk Zahn,[‡] Andreas Hirsch,[⊥] Marcus Halik,[*,§] and Timothy Clark[*,†]

[†]Computer-Chemie-Centrum and Interdisciplinary Center for Molecular Materials, and [‡]Chair of Theoretical Chemistry, University Erlangen-Nürnberg, Nägelsbachstrasse 25, 91052 Erlangen, Germany

[§]Organic Materials & Devices, Institute of Polymer Materials, Department of Materials Science, University Erlangen-Nürnberg, Martensstrasse 7, 91058 Erlangen, Germany

[∥]European Synchrotron Radiation Facility (ESRF), 6 rue Jules Horowitz BP220, 38043 Grenoble Cedex, France

[⊥]Chair of Organic Chemistry II, University Erlangen-Nürnberg, Henkestrasse 42, 91054 Erlangen, Germany

Supporting Information

ABSTRACT: A three-pronged approach has been used to design rational improvements in self-assembled monolayer field-effect transistors: classical molecular dynamics (MD) simulations to investigate atomistic structure, large-scale quantum mechanical (QM) calculations for electronic properties, and device fabrication and characterization as the ultimate goal. The MD simulations reveal the effect of using two-component monolayers to achieve intact dielectric insulating layers and a well-defined semiconductor channel. The QM calculations identify improved conduction paths in the monolayers that consist of an optimum mixing ratio of the components. These results have been used both to confirm the predictions of the calculations and to optimize real devices. Monolayers were characterized with X-ray reflectivity measurements and by electronic characterization of complete devices.

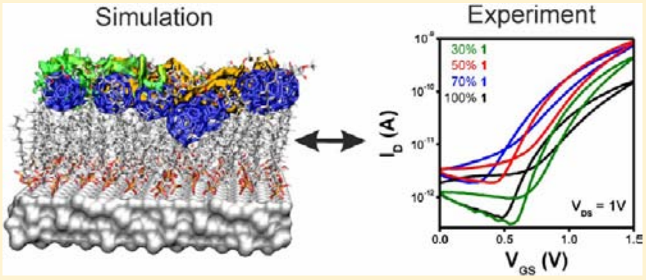

INTRODUCTION

In addition to their enormous application potential in circuits, backplane drivers, sensors, or memories,[1−5] organic thin film transistors represent an exciting new challenge for both theory and experiment. Experimentally, diverse and mutually unfamiliar disciplines such as organic synthesis, surface chemistry, and materials science become eminently important for device fabrication. Theoretically, the challenge of adequate conformational sampling of flexible electronically active molecules adds a new dimension to modeling electronic devices, which can no longer be treated statically, but rather as dynamic ensembles of conformations. In particular, the charge transport, essentially limited to the first closed monolayer[6−8] at the dielectric−semiconductor interface, critically depends on effective molecular arrangement of the π-systems to form conductive pathways. While adequate conformational sampling only plays a small role in small-molecule modeling, it becomes the dominant aspect for macromolecules, so that the quality of the simulation is dictated by the need for extensive sampling. However, classical molecular-dynamics (MD) techniques are of limited use in simulating organic electronics devices because they treat the electrons implicitly in what is essentially a coarse-grained ansatz designed to mimic quantum mechanics. It is therefore necessary either to perform direct quantum mechanical MD (e.g., Car−Parrinello density-functional theory (DFT)-based MD) or to use a multiscale treatment in which the MD (i.e., the conformational sampling) is performed classically and the geometries of "snapshots" from the classical MD-simulation used for hundreds of single-point quantum mechanical calculations to determine the electronic properties from these conformational ensembles. We chose the latter approach as it allows both extensive statistical sampling over hundreds of nanoseconds and a posteriori quantum chemical characterization on snapshots including up to 16 000 atomic orbitals. A further challenge in modeling such systems is that the mechanism of charge transport is not uniquely defined in terms of the traditional concepts of metallic conductance, resonant coherent charge transfer, or hopping because the exact nature of the electronic system (delocalized, localized electron or hole traps, etc.) may vary from region to region of the disordered organic system. Typically, such organic systems are also characterized by a myriad of closely spaced energy levels, so that in particular a simple two-state cannot be used reliably. We have therefore decided in a first step to use a simple quantitative visualization technique[9] to help characterize the

Received: February 5, 2013
Published: March 12, 2013

dx.doi.org/10.1021/ja401320n | *J. Am. Chem. Soc.* 2013, 135, 4893−4900

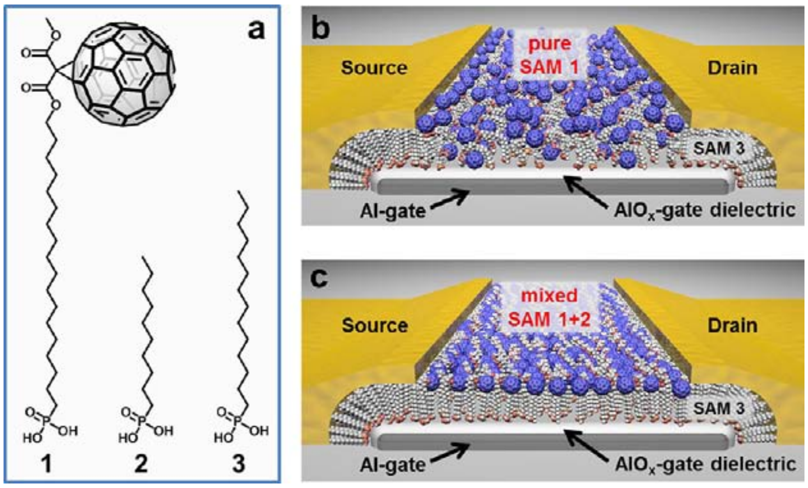

Figure 1. Schematic and chemical composition of SAMFET devices. (a) Chemical structure of the SAM forming phosphonic acids $C_{60}C_{18}$-PA (**1**), C_{10}-PA (**2**), and C_{14}-PA (**3**) underneath source and drain electrodes. (b,c) Schematic SAMFET setups (details of device preparation are given in the Supporting Information).

electronic properties of the SAMs. This technique, which is based on the concept of the local electron affinity,[10,11] allows us to consider all accessible energy levels in a space-resolved fashion without prejudicing the results by assuming a single charge-transport mechanism.

Self-assembled monolayer field-effect transistors (SAMFETs) provide an excellent system for investigating the dependency of transport properties on the molecular order and molecular composition of the first monolayer, because the active transport layer is intrinsically confined and limited to one molecular layer in thickness. In such a challenging field, theory and experiment can profit strongly from each other; theory can provide atomistic details of the devices that are not accessible experimentally, and experiment poses questions for which there are no established theoretical treatments.

The molecules that comprise the SAM contain insulating and semiconducting moieties, so that they serve as both gate dielectric and the active transistor channel in a device.[12] They can be fabricated in a self-aligned and self-terminated one-step solution process, due to their asymmetric substitution with a surface selective anchor group.[12−14] Typically, an effective charge transport is dedicated to an optimized interaction of the donor or acceptor levels of adjacent molecules in the channel.[15] In classical organic field-effect transistors (OFETs), where the semiconductor consists of a polycrystalline film, a single crystal of small molecules or of thin polymer layers, the favorable crystalline molecular arrangement is driven by intermolecular $\pi\pi$-stacking and surface interaction that help control the orientation of the crystalline domains.[16−18] To date, the orientation and morphology of the first monolayers formed during deposition can be tuned but cannot be predicted reliably in experiment or by theory.[17,19] In SAMFETs, the molecular arrangement is basically determined by two parameters, the packing density of the molecules and their shape. Both p- and n-type SAMFETs have recently been realized. Specifically synthesized molecules with acene-, thiophene-, perylene bisimide-, or C_{60}-semiconducting components were self-assembled as one-component monolayers.[14,20−24] Devices based on C_{60} have great potential for improving device performance by increasing the molecular order. In contrast to flat π-conjugated semiconductor units, where the transport critically requires an effective 2D-crystalline $\pi\pi$-stacking,[18] the C_{60}−C_{60} interaction is expected to be less sensitive to molecular orientation because of the spherical molecular shape. On the other hand, the relatively large diameter (~1 nm) of the C_{60} motif represents a mismatch to the tiny alkyl chain and anchor group, so that we cannot expect a fully ordered and densely packed monolayer, in which the molecular anchor group saturate the binding sites on the surface. Charge transport across the semiconductor layer, and thus device operation, are therefore influenced strongly by the conformation and structure of the SAM. Using more than one type of molecule in a multicomponent SAM is a promising approach to being able to control the structure and morphology.[25] Bain et al. demonstrated the formation of a two-component mixed SAM by a coadsorption process from stoichiometric solutions.[26,27] The mixing ratio and molecular composition of the SAMs provide two tunable variables for controlling the morphology and SAM characteristics.[28] Mixed phosphonic acids were shown to self-assemble to homogeneous and randomly distributed mixed monolayers (no phase separation) whose composition is determined by the stoichiometric ratios of the molecules in solution.[5,29−32]

In this Article, we address the question of how the performance of a real SAMFET-device can be related to the morphology and the molecular arrangement of the SAM. We have investigated pure monolayers of functionalized octadecylphosphonic acids, $C_{60}C_{18}$-PA **1**, and mixed monolayers of **1** and C_{10}-PA, **2** (Figure 1), in various stoichiometric ratios (70:30, 50:50, and 30:70) by simulation and as active monolayers in SAMFET devices. We report combined theoretical and experimental investigations in which simulations play an integral role in designing optimal SAMs and testing hypotheses such as those derived from cartoons like Figure 1b,c. Classical molecular-dynamics (MD) simulations and semiempirical molecular orbital (MO) theory were used to simulate the SAM morphology and the related electronic structure. We have used Monte Carlo approaches to identify preferred electron-transport pathways, which depend strongly on the SAM morphology. The SAM morphology was investigated by X-ray reflectivity measurements (XRR) and electrical device measurements in addition to the theoretical investigations.

Table 1. Composition of SAMs in MD Simulations

simulation	% of **1**	surface coverage [nm^{-2}]	molecules per periodic cell [1:2]	accessible layer thickness [nm]^a	mean fullerene distance to substrate [nm]
MD100%	100	0.9	25:0	1.22 ± 0.44	0.95 ± 0.31
MD25%	25	3.6	25:75	2.00 ± 0.50	1.74 ± 0.25
MD33%	33	2.7	25:50	1.75 ± 0.48	1.44 ± 0.30
MD38%	38	2.3	25:40	1.56 ± 0.51	1.35 ± 0.33
MD50%	50	1.8	25:25	1.45 ± 0.39	1.14 ± 0.28

^{a}The mean accessible layer thickness is calculated from the averaged surface accessible by a sphere with a radius of 0.2 nm. The averaged surface was calculated from 80 ns simulation, taking snapshots every 50 ps.

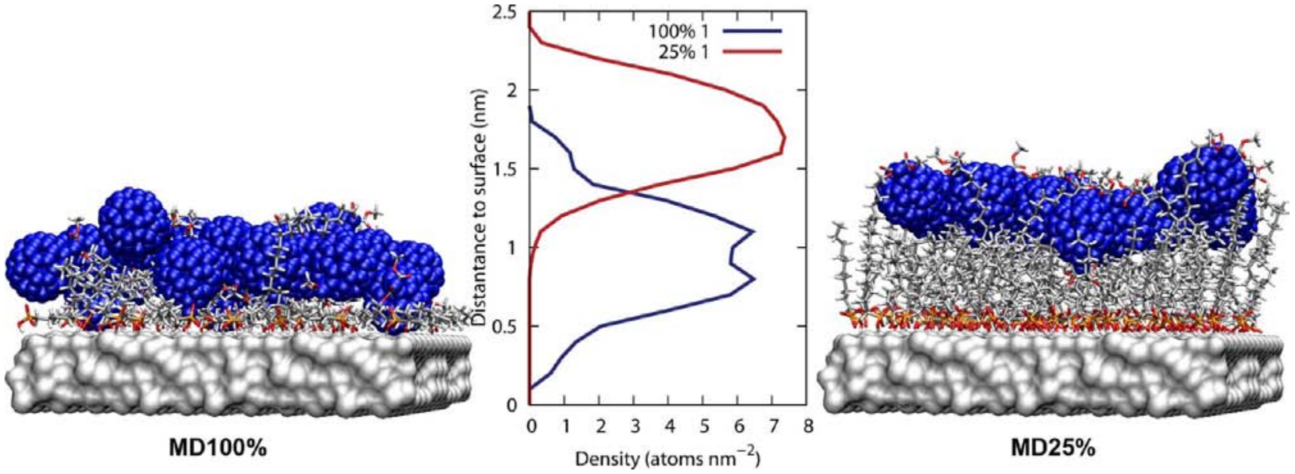

Figure 2. SAM morphology derived from MD. Snapshots of the molecular conformation of pure **1** and 25:75 mixed SAM after a simulation time of 50 ns. Fullerene head-groups are shown in blue. Average fullerene atom density from 80 ns simulation time in pure **1**, 25% mixed SAM (the results for other concentrations are shown in Figure S1 of the Supporting Information).

■ RESULTS AND DISCUSSION

Molecular-Dynamics Simulations. Figure 1 shows schematic thin film transistor (TFT) setups in which the active channel and the insulating dielectric consist of SAMs of either pure **1** (Figure 1b) or a mixture of **1** and **2** (Figure 1c). We used classical atomistic molecular-dynamics simulations to investigate the dynamic structure of the mixed monolayers. These simulations provide information about the role and importance of the SAM's morphology and can be used to determine the influence of this morphology on the electrical characteristics of the devices.

Table 1 summarizes the simulations performed. Starting from an ideally densely packed pure monolayer of **2** with a surface coverage of 3.6 molecules per square nanometer, molecules of **2** were replaced by **1** to give a densely packed and ordered starting configuration without intermolecular clashes of the same surface coverage. This leads to a mixed SAM with a content of 25% **1** (MD25%). To investigate the effect of lower concentrations of **2**, molecules of **2** were removed from the initial setup (MD29%−MD50%), resulting in less dense SAMs with a higher concentration of **1**. Details of the procedure used are given in the Supporting Information.

A comparison of simulations on the pure SAM composed of **1** (MD100%) and the mixed SAM MD25% reveals large differences in their morphology (see Figure 2). From the outset of simulation MD100%, the molecules begin to reorganize on the surface. The long and flexible alkyl chain of **1** (~2.5 nm) allows the molecules to twist, lie on, or protrude from the surface. Within the first nanosecond, the initially stretched molecules collapse and sink onto the substrate. The resulting monolayer has considerably reduced thickness with a broad and disordered occupancy of C_{60} and a mean distance of the C_{60} atoms to the surface of 0.95 ± 0.31 nm (Table 1; Figure 2). The C_{18}-chains of **1** collapse almost fully, yielding no pronounced insulating alkyl layer. A different result is observed for MD25% with a 1:3 ratio of **1** and **2**. Molecules **2** with an *n*-alkyl chain length of 1.4 nm were incorporated below the bulky C_{60} head groups and occupy free sites on the AlO_x substrate. During the simulation (supplementary video available), this supporting layer of **2** stabilizes the molecules of **1** and prevents them from collapsing onto the substrate. Sporadically, fullerenes sink into the lower layer of **2**, but most molecules of **1** remain well aligned, as was also indicated by a smaller decrease of the mean inclination angle of the alkyl chains of **1** relative to the surface (from 80° in the starting structure to 56° at 100 ns as compared to 18° for MD100%). The resulting MD morphology (Figure 2) indicates a significant insulating layer of 1.2 nm below the C_{60} motif. This value is still smaller than the 2.5 nm maximum length of the C_{18} alkyl chain in **1** but comparable to that of C_{10}-PA **2**. An increased mean distance to the surface of 1.74 nm was obtained together with a sharp distribution of the C_{60} (rmsd 0.25 nm) within the layer. Comparable results were obtained for other mixing ratios (see Supporting Information Table S1).

SAM Morphology by XRR Experiments. To validate the results of the MD simulations, we have performed XRR experiments at the beamline ID10 at the ESRF (Grenoble, France) with a SAM of pure **1** and mixed SAMs of **1** and **2** (mixing ratio 30:70) on atomic layer deposition (ALD) grown AlO_x. The SAM deposition followed the same procedure as used for device fabrication. Best fit scattering length density (SLD) profiles and the reconstructed SAM morphologies are

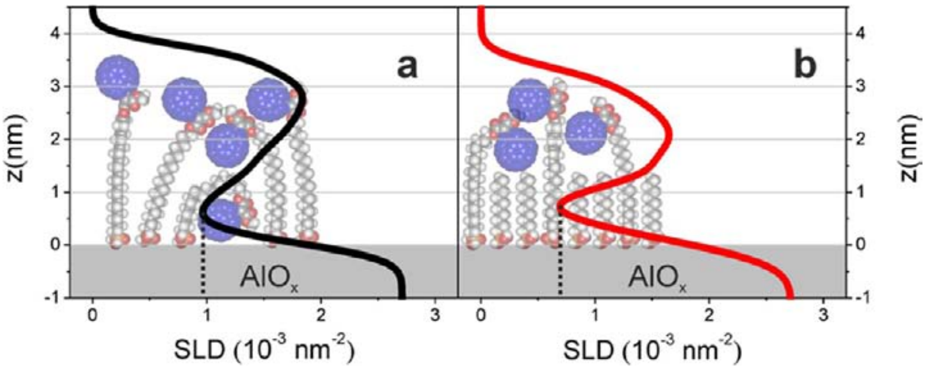

Figure 3. XRR measurements. Best fit SLD profiles from XRR experiments of pure **1** (a) and mixed SAMs of 30% **1** and 70% **2** (b) on ALD grown AlO$_x$.

shown in Figure 3. Profiles of the two different SAMs show one important difference. Whereas the two-component SAM exhibits a pronounced insulating layer of about 1.2 nm close to the surface with a typical SLD value of 0.7×10^{-3} nm^{-2} (Figure 3b), the pure SAM of **1** shows a value of about 1×10^{-3} nm^{-2}, indicating the presence of π-electrons close to the AlO$_x$-surface (Figure 3a). The SAM thickness is approximately 3.5 nm, in good agreement with the length of a stretched molecule **1**. The distribution of high SLD carbon (C_{60}) occurs over 2.5 nm for the mixed SAM, indicating that the C_{60} head groups arrange as an "amorphous" layer of nominally two C_{60} units thickness on top of the insulating C_{10} layer. The pure SAM **1** exhibits a broader C_{60} region (~3.0 nm), an overall thickness close to that found for the mixed SAM, and a significantly higher SLD minimum 0.5 nm above the surface that indicates some density of fullerene groups close to the surface. The mixed SAM exhibits a lower value for this local SLD minimum (0.7×10^{-3} as compared to 1.0×10^{-3} nm^{-3}) slightly further away from the surface (0.75 as compared to 0.60 nm). These features are reproduced by the simulations, even though the thickness of the SAM is not.

Thus, the overall layer thickness obtained from the XRR experiments does not match that found in the MD simulation perfectly. However, this deviation was expected because of the differences in the physical systems found in the experiment and used for the simulations. The starting structures for the MD simulations are constrained to a single bound monolayer, which is limited by the number of molecules that can be accommodated by a densely ordered packed C_{60} layer. In experimental SAM deposition from solution, all accessible vacancies on the AlO$_x$ surface will likely be occupied by the PA anchor groups because the conformationally flexible molecules can rearrange to allow access to others. This process leads to a higher density of C_{60} molecules in the SAM (as found in the XRR), whereby the additionally adsorbed molecules extend the SAM with a disordered amorphous second and third C_{60} layer until the monolayer formation self-terminates. This is compatible with the results of the simulations because the inclination of the SAM-molecules relative to the surface is quite flat (18°), resulting in a maximum concentration of C_{60} quite close (1.5–2 nm) to the oxide surface. Less ordered SAMs can contain more extended molecules at steeper angles to the surface, so that additional layers of C_{60} can be accommodated up to the fully extended distance of approximately 3 nm. Further MD simulations with higher C_{60} densities support this interpretation as they show a thickness comparable to that of the XRR experiments, but amorphous fullerene distribution similar to the MD100% simulation (see Supporting Information Figure S2 for details).

In this work, however, we have only considered the contiguous C_{60} layer closest to the interface for the calculations on charge transport. This is adequate for our present purposes because leakage paths to the oxide surface start in this layer.

Semiempirical MO Calculations. The semiempirical MO calculations were used to construct three-dimensional maps of the electron density and the local electron affinity[10,11] in the SAM-snapshots. Time-averaged maps were constructed by summing and averaging. The change of the electron density in the SAM as a function of the height above the surface is shown in Supporting Information Figure S3. It shows regions of high electron density that correspond to the geometrical location of the fullerenes as observed directly in the MD simulations.

The local electron affinity is defined[10,11] as

$$EA_L = \frac{\sum_{i=\mathrm{LUMO}}^{\mathrm{norbs}} -\rho_i \varepsilon_i}{\sum_{i=\mathrm{LUMO}}^{\mathrm{norbs}} \rho_i} \tag{1}$$

where LUMO is the lowest unoccupied molecular orbital (MO), norbs is the number of MOs, ρ_i is the electron density attributed to the ith MO at the point being considered, and ε_i is the eigenvalue of MO i. It is in effect a density-weighted electron affinity, or in the present context represents the local lower edge of the conductance band. It has been used previously to visualize electron-transfer paths in donor–bridge–acceptor conjugates.[9] Because use of the local electron affinity (EA_L) is not common in this field, some additional expalnations are useful. First, the definition given in eq 1 involves a sum over all virtual orbitals. This sum is inifinite in a complete basis set and will contain many unwanted diffuse orbitals or polarization functions in most adequate bases. However, traditional NDDO-based semiempirical molecular orbital techniques, such as AM1[33] used here, employ a minimal s,p-basis set of Slater atomic orbitals. In such cases, the sum of eq 1 is limited to valence-like orbitals, which gives a good representation of the conductance levels. For techniques such as MNDO/d[34] or AM1*[35] that use d-orbitals as polarization functions, the simple intensity-filtering technique defined in ref 9 limits the sum to valence-like orbitals. A further important characteristic of the local electron affinity is that, although it is conceptually similar to the Fukui function,[36] it is not limited to the frontier orbitals (in this case the lowest unoccupied molecular orbital, LUMO) but extends over all valence-like virtual orbitals. Thus, it is well suited for systems such as those considered here in which many acceptor levels are close in

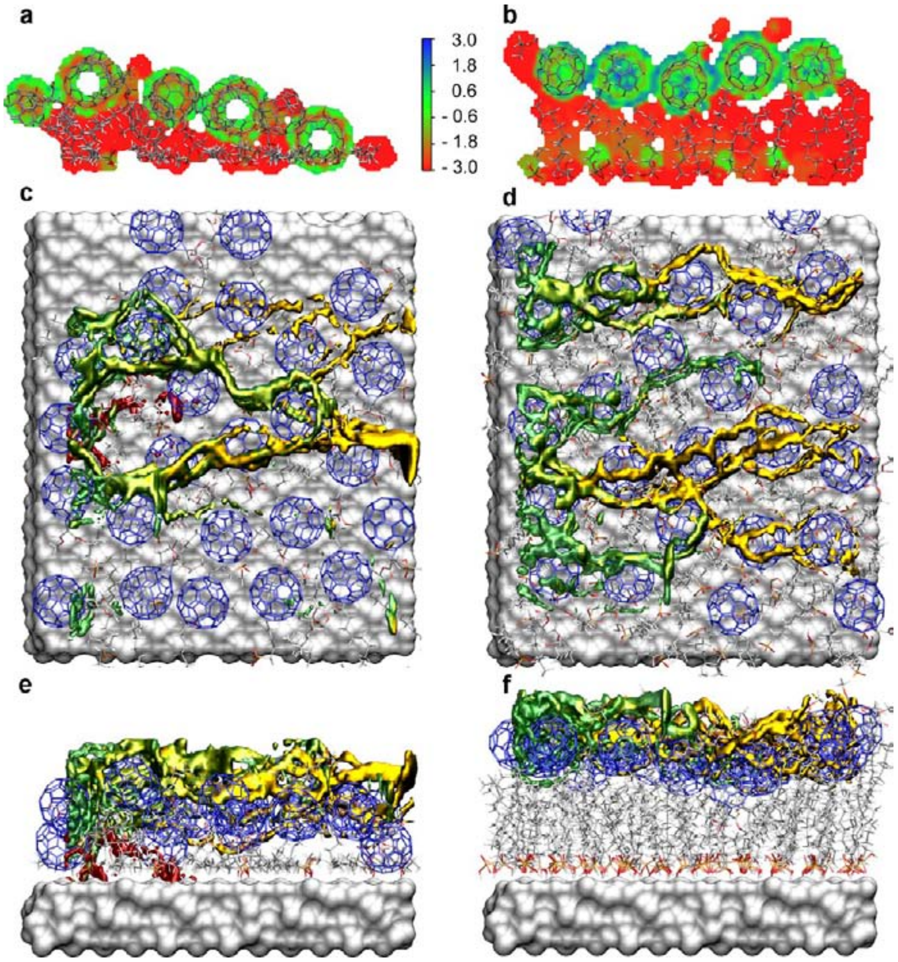

Figure 4. Local electron affinity and Metropolis Monte Carlo paths. Slices through the local electron affinity map for snapshots taken after 50 ns of MD100% (a) MD25% (b). Units of the color scale bar are in electronvolts. (c−f) Monte Carlo electron transfer paths through the same snapshots (top (c,d) and side views (e,f)). Green paths terminating in the SAM, red paths terminating on the AlO_x surface, and golden paths crossing the snapshot. MC simulation carried out at kT = 285 mV. See also the Supporting Information for more details.

energy. Similarly, the 3D-distribution of the local electron affinity can provide information about all three types of charge transport outlined above. Either metallic or conjugative delocalization will be reflected in a continuous path of low-energy (more positive local electron affinity), whereas electron traps will be clearly visible as low-lying basins in EA_L separated by barriers whose height is determined by geometrical (distance) factors rather than coupling integrals and vertical excitation energies, but will nonetheless be a reasonable representation of the traditional curve-crossing picture of two-state Marcus theory. The density-weighting procedure used to determine the EA_L (eq 1) is not physically equivalent to a curve-crossing between two states, but barriers of more negative EA_L are found in the paths between basins (electron traps). We are currently investigating the significance of these barriers on constructed model systems for which we can calculate curve-crossing barriers.

The local electron affinity as a function of the distance above the substrate is also shown in the Supporting Information for the different simulations. As expected, the fullerenes correspond to the areas of highest (most positive) local electron affinity. Because EA_L has been time-averaged, it remains negative (electrons are not bound relative to vacuum) throughout, although the value on the surface of the fullerenes is significantly positive (up to 1.38 eV for a single fullerene). A detailed view of slices through the electron affinity maps for individual snapshots selected at random from MD100% and MD25% emphasizes the differences (Figure 4a,b). While MD25% shows continuous paths of high electron affinity, the pure SAM reveals breaks in the n-type conductance path (Figure 4a).

To identify and visualize electron-transfer paths through snapshots of the SAM, we performed path searches using the EA_L map divided into pixels (grid points) as the energy function. Paths were initialized randomly on either side of the SAMs and allowed to progress from pixel to pixel through the system on the basis of a simple Metropolis Monte Carlo approach. To search for continuous paths that travel from one side of the simulations system to the other, steps backward were not allowed. Thus, the algorithm represents a simple directed path search in which paths can be initiated at an "electrode" and are classified as to whether they reach the other "electrode", remain trapped in the SAM, or contact the oxide surface. The energy profiles along the path can display barriers between electron traps or may remain flat, approximating electron hopping or delocalized electron transport. There may be one or many barriers along a path, differentiating between a single resonant transfer event and hopping. Thus, although simple to calculate and not quantitative, charge-transport paths based on a 3D-EA_L map provide a powerful one-electron

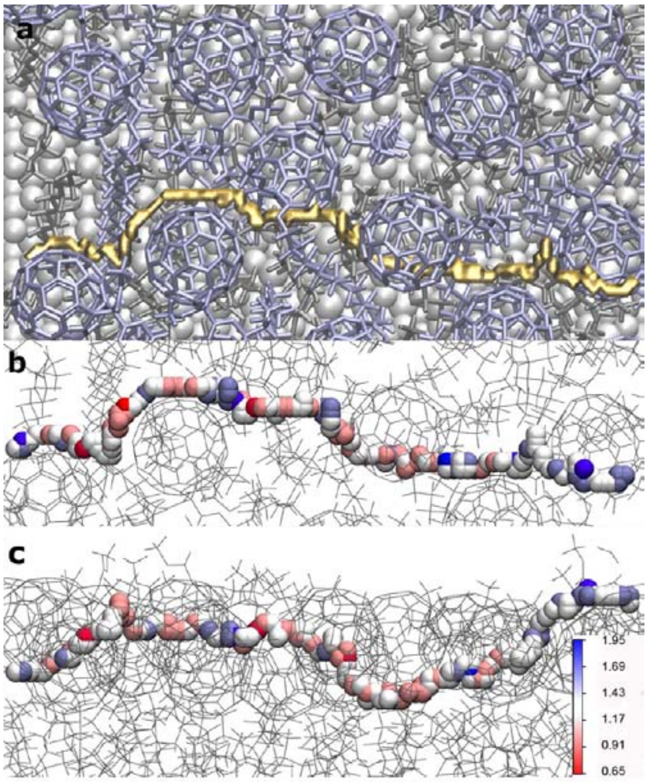

Figure 5. Selected MC path with most positive (=most stable) EA_L profile from a snapshot of MD25% after 25 ns simulation time depicting a number of energetically favored basins (blue) and barriers (red) in close proximity. (a) Top view on the SAM, path shown in golden. (b,c) Top and side views of the same path. Path colored by EA_L values. Energy values are given in electronvolts.

picture of charge transport in complex systems. Figure 5 illustrates the path with the highest EA_L profile for a snapshot of MD25% and depicts energy barriers and basins both lying in between adjacent fullerene moieties.

Figure 4c–f shows paths determined at the same Monte Carlo temperature for snapshots of MD100% and MD25%. A large majority of the paths are trapped in the system because no driving force is included in these simulations. However, those paths that reach their destination show qualitative examples for conducting paths through this amorphous and disordered semiconductor. Moreover the simulation shows large differences for MD25% and MD100%. Clearly, more paths terminate either in the SAM or even on the substrate in the case of MD100%, suggesting poorer conducting properties.

Although, as outlined above, these paths simply visualize one-electron paths within a single snapshot, they display the expected qualitative increase in conductance with Monte Carlo simulation temperature and provide a basis for more physically correct models for conduction in flexible semiconductor aggregates. The findings suggest that electron transport is more efficient in mixed SAMs due to confined and more effective pathways. To test these conclusions, we have measured the electron transport of corresponding SAMs in self-assembled monolayer field-effect transistors.

Electronic Characterization. The molecular self-assembly of pure and stoichiometrically mixed monolayers of **1** and **2** was performed on prepatterned substrates fabricated on SiO_2 wafers (see the Supporting Information for details) with free access to the channel region, which is based on an AlO_x layer with a surface roughness of rms = 1.3 nm. To have a constant source gate capacitance and a low gate leakage current (I_G), the source-gate overlap (3 μm) was created from C_{14}-PA **3** (Figure 1a) as highly insulating SAM.[37] Schematic images of devices with pure and mixed SAM are shown in Figure 1b and c, respectively. All devices exhibit a channel length (L) of 3 μm and a channel width (W) of 100 μm and were electrically characterized in inert atmosphere. Figure 6c shows the output characteristics of representative SAMFETs with pure SAM of **1** and mixed SAMs of **1** and **2** in mixing ratios of 30:70, 50:50,

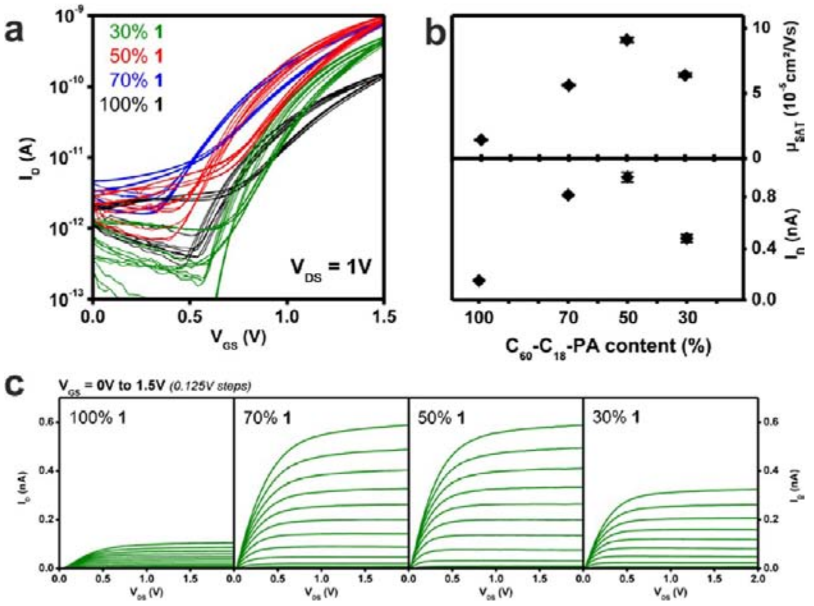

Figure 6. Electrical characterization of SAMFET devices. (a) Electrical transfer characteristics of SAMFET devices with different SAM mixing ratios (three devices each). (b) Summary of saturation mobility and maximum drain current related to the content of **1**. (c) Representative output characteristics of SAMFET devices for different channel compositions.

and 70:30. The pure SAM of **1** (Figure 6a) exhibits typical n-type behavior with pronounced gate modulation and a maximum drain current of 0.15 nA. By increasing the mixing ratio to 30:70 and 50:50, the general n-type characteristics remain, but we obtained an increased I_D of 0.8 and 0.9 nA (Figure 6b). We note that all values are highly reproducible with small deviations (Figure 6a,b). Further increasing the amount of **2** leads to a slightly reduced I_D of 0.45 nA, but it is still above the value of the pure SAM of **1**. Devices with concentrations of **1** lower than 30% show no gate modulation. We assign this effect to disconnected pathways of the C_{60} motifs.[5] We obtained an increased mobility by almost 1 order of magnitude at a mixing ratio of 50:50 as compared relative to the devices with the pure SAM **1** as active channel, which shows that even with nominally diluted active head groups, the transport is more effective. We believe that this effect is due to an improved morphology, which yields more effective pathways for the electron transport as described by the simulations. The optimum mixing ratio of 50:50 in our devices is slightly shifted to a lower content of **2** than that suggested by the simulations (75%), but still strongly confirms the trend found in the simulations. We suggest that this shift is caused by the extreme surface roughness in our devices as compared to the ideal flat surface in the simulations and to differences in the surface coverage.

■ CONCLUSION

In summary, we have shown that a combined approach of MD simulations, electronic structure calculations, Monte Carlo simulation, and device fabrication and characterization enables us to describe and optimize complex systems of self-assembled monolayers on surfaces, not only to explain their morphology but also to predict molecular compositions and arrangements favorable for improved charge transport. The results of the simulations agree well with real device characteristics, confirming that simulations on models of several nanometers dimension can be predictive for real devices of several micrometers.

Both simulations and experiment demonstrate that a mixture of functionalized and nonfunctionalized spacer molecules can lead to a morphology in which a consistent and continuous semiconductor layer clearly separated from the gate electrode by an effective insulator layer.

Although the simulations of a single SAM layer at surface coverages up to 2.6 molecules nm^{-2} underestimate the thickness of the layer as compared to that observed in the XXR experiments, increasing the coverage results in better agreement with experiment, as shown in the Supporting Information.

■ METHODS

Molecular Dynamics. The molecules were initially aligned on a clean aluminum-oxide surface analogously to previous work.[37] The surface (0001) is represented by an aluminum terminated slab (4.9 × 5.7 nm), which was equilibrated prior to the deposition of phosphonic acids using an interatomic potential model parametrized by Sun et al.[38] The parameters for the phosphonic acids are based on the general Amber force field (GAFF).[39] The acids were treated as being singly deprotonated, and the surface atoms were constrained in their positions during the simulation. MD simulations were performed with the program DL-POLY[40] on systems of pure and mixed monolayers of **1** and **2** in different concentrations. Each system was minimized, equilibrated, and simulated in vacuo with periodic boundary conditions for a simulation time of 100 ns with an integration time step of 1 fs. Constant volume dynamics (NVT) were applied, and the electrostatic interactions were treated using the particle mesh Ewald (PME) method[41] and a 1.2 nm distance cutoff for nonbonded interactions (see also the Supporting Information for details).

Monte Carlo and Semiempirical Calculations. Semiempirical (AM1)[33] molecular orbital calculations were used to investigate the electronic properties of the monolayers using an ensemble model based on snapshots taken from the MD simulations.[42] The calculations used the restricted Hartree−Fock formalism on snapshot geometries taken from the equilibrated simulations (after 25 ns equilibration) every 500 ps to give a total of 150 snapshots of each system. The structures used for the calculations consisted of the SAM alone without the Al_2O_3 layer. The phosphonates were protonated to give a neutral system overall. Semiempirical MO calculations were performed using the parallel EMPIRE program.[43]

Metropolis Monte Carlo (MC) path searches were using the EA_L maps as the energy function. Paths were initialized randomly on all four sides of the SAMs to mimic possible source drain paths in all directions. The EA_L maps were truncated by 15% on either side of the systems, to avoid boundary effects. In total, 40 000 paths were initialized in any calculation at randomly chosen starting positions with positive EA_L values only. Each step corresponds to a random step on the three-dimensional EA_L map with the restrictions for each path not to visit the same position twice and not to move in the direction of the source. A path is considered trapped when the Metropolis test fails for the hundredth time at the same position. For each snapshot, the MC path searches were carried out for 25 different MC temperatures (1000−3500 K).

Device Fabrication. For device fabrication, 30 nm aluminum was thermally evaporated onto silicon wafers with 100 nm thermal oxide and patterned by standard photolithographical methods to form the gate structures. To obtain a dense aluminum oxide layer, an oxygen plasma treatment was performed (Diener Electronic Pico, 200 W, 0.2 mbar, 5 min). Subsequently, a monolayer of **3** was self-assembled by immersion into a 0.2 mM solution of **3** in 2-propanol for 72 h, as described before.[44] 30 nm gold was thermally evaporated on top of the SAM decorated gate electrodes and lithographically patterned to serve as source and drain electrodes. The C_{14}-PA was removed from the channel area by an oxygen plasma treatment (conditions as described above) to assemble the active SAMs. Because of the masking of the Au pattern, the SAM is only removed in the channel but remains beneath source and drain contacts, providing the same source gate capacitance in all devices. To self-assemble the active monolayer, substrates were immersed into mixed solutions of **1** and **2** (containing 100%, 70%, 50%, or 30% **1**) with overall concentrations of 0.005 mM in 2-propanol for 72 h, rinsed with 2-propanol, dried on a hot plate (60 °C, 3 min), and transferred into a glovebox. All devices were annealed at 120 °C for 20 h and electrically characterized. Transfer characteristics were measured for gate voltages (V_{GS}) from 0 to 1.5 V with constant source-drain voltages (V_{DS}) of 1 V. For output measurements, V_{DS} was varied from 0 to 2 V with fixed V_{GS}, which was modified from 0 to 1.5 V in 0.125 V steps. Charge carrier mobilities in the saturation regime were calculated from the slope of the $\sqrt{I_D}$ versus V_{GS} curve for a capacitance of 0.86 $\mu F/cm^2$ according to the literature.[45]

X-ray reflectivity measurements were carried out at the beamline ID10 at the ESRF (Grenoble, France) using a monochromatic X-ray beam with photon wavelength $\lambda = 1.55$ Å. Specularly reflected X-rays and parasitic background were collected with a linear position sensitive detector. After background correction and normalization on the intensity of the incoming beam I_0, reflectivity data were fitted to a model scattering length density profile using the Parratt formalism.[46] The best SLD profile was identified by a least-squares fit analysis.

■ ASSOCIATED CONTENT

Ⓢ Supporting Information

Additional figures, tables, experimental procedures, and simulation details. This material is available free of charge via the Internet at http://pubs.acs.org.

■ AUTHOR INFORMATION

Corresponding Author

marcus.halik@ww.uni-erlangen.de; tim.clark@chemie.uni-erlangen.de

Notes

The authors declare no competing financial interest.

■ ACKNOWLEDGMENTS

We acknowledge the German Research Council (DFG), the Collaborative Research Center 953, the Cluster of Excellence “Engineering of Advanced Materials – EXC 315” (www.eam.uni-erlangen.de), HA 2952/4-1, the Erlangen Graduate School of Molecular Science (GSMS), the Interdisciplinary Center for Molecular Materials (ICMM), and the ESRF for financial support.

■ REFERENCES

(1) Klauk, H.; Zschieschang, U.; Pflaum, J.; Halik, M. *Nature* **2007**, *445*, 745−748.

(2) Sekitani, T.; Yokota, T.; Zschieschang, U.; Klauk, H.; Bauer, S.; Takeuchi, K.; Takamiya, M.; Sakurai, T.; Someya, T. *Science* **2009**, *326*, 1516−1519.

(3) Gelinck, G. H.; Huitema, H. E. A.; van Veenendaal, E.; Cantatore, E.; Schrijnemakers, L.; van der Putten, J. B. P. H.; Geuns, T. C. T.; Beenhakkers, M.; Giesbers, J. B.; Huisman, B.-H.; et al. *Nat. Mater.* **2004**, *3*, 106−110.

(4) Sekitani, T.; Zschieschang, U.; Klauk, H.; Someya, T. *Nat. Mater.* **2010**, *9*, 1015−1022.

(5) Burkhardt, M.; Jedaa, A.; Novak, M.; Ebel, A.; Voïtchovsky, K.; Stellacci, F.; Hirsch, A.; Halik, M. *Adv. Mater.* **2010**, *22*, 2525−2528.

(6) Mottaghi, M.; Horowitz, G. *Org. Electron.* **2006**, *7*, 528−536.

(7) Tanase, C.; Meijer, E. J.; Blom, P. W. M.; de Leeuw, D. M. *Org. Electron.* **2003**, *4*, 33−37.

(8) Brondijk, J. J.; Roelofs, W. S. C.; Mathijssen, S. G. J.; Shehu, A.; Cramer, T.; Biscarini, F.; Blom, P. W. M.; de Leeuw, D. M. *Phys. Rev. Lett.* **2012**, *109*, 056601.

(9) Atienza, C.; Martin, N.; Wielopolski, M.; Haworth, N.; Clark, T.; Guldi, D. M. *Chem. Commun.* **2006**, 3202−3204.

(10) Ehresmann, B.; Martin, B.; Horn, A. C.; Clark, T. *J. Mol. Model.* **2003**, *9*, 342−347.

(11) Clark, T. *J. Mol. Model.* **2010**, *16*, 1231−1238.

(12) Novak, M.; Schmaltz, T.; Faber, H.; Halik, M. *Appl. Phys. Lett.* **2011**, *98*, 093302.

(13) Halik, M.; Hirsch, A. *Adv. Mater.* **2011**, *23*, 2689−2695.

(14) Smits, E. C. P.; Mathijssen, S. G. J.; van Hal, P. A.; Setayesh, S.; Geuns, T. C. T.; Mutsaers, K. A. H. A.; Cantatore, E.; Wondergem, H. J.; Werzer, O.; Resel, R.; et al. *Nature* **2008**, *455*, 956−959.

(15) Knipp, D.; Street, R. A.; Volkel, A.; Ho, J. *J. Appl. Phys.* **2003**, *93*, 347−355.

(16) Sirringhaus, H.; Brown, P. J.; Friend, R. H.; Nielsen, M. M.; Bechgaard, K.; Langeveld-Voss, B. M. W.; Spiering, A. J. H.; Janssen, R. A. J.; Meijer, E. W.; Herwig, P.; et al. *Nature* **1999**, *401*, 685−688.

(17) Weitz, R. T.; Amsharov, K.; Zschieschang, U.; Villas, E. B.; Goswami, D. K.; Burghard, M.; Dosch, H.; Jansen, M.; Kern, K.; Klauk, H. *J. Am. Chem. Soc.* **2008**, *130*, 4637−4645.

(18) Sundar, V. C.; Zaumseil, J.; Podzorov, V.; Menard, E.; Willett, R. L.; Someya, T.; Gershenson, M. E.; Rogers, J. A. *Science* **2004**, *303*, 1644−1646.

(19) Anthony, J. E. *Angew. Chem.* **2008**, *120*, 460−492.

(20) Ringk, A.; Xiaoran, L.; Gholamrezaie, F.; Smits, E. C. P.; Neuhold, A.; Moser, A.; van der Marel, C.; Gelinck, G. H.; Resel, R.; de Leeuw, D. M.; et al. *Adv. Funct. Mater.* **2012**, 1616−3028.

(21) Mathijssen, S. G. J.; Smits, E. C. P.; van Hal, P. A.; Wondergem, H. J.; Ponomarenko, S. A.; Moser, A.; Resel, R.; Bobbert, P. A.; Kemerink, M.; Janssen, R.; et al. *Nat. Nano* **2009**, *4*, 674−680.

(22) Novak, M.; Ebel, A.; Meyer-Friedrichsen, T.; Jedaa, A.; Vieweg, B. F.; Yang, G.; Voitchovsky, K.; Stellacci, F.; Spiecker, E.; Hirsch, A.; et al. *Nano Lett.* **2010**, *11*, 156−159.

(23) Guo, X.; Myers, M.; Xiao, S.; Lefenfeld, M.; Steiner, R.; Tulevski, G. S.; Tang, J.; Baumert, J.; Leibfarth, F.; et al. *Proc. Natl. Acad. Sci. U.S.A.* **2006**, *103*, 11452−11456.

(24) Tulevski, G. S.; Miao, Q.; Fukuto, M.; Abram, R.; Ocko, B.; Pindak, R.; Steigerwald, M. L.; Kagan, C. R.; Nuckolls, C. *J. Am. Chem. Soc.* **2004**, *126*, 15048−15050.

(25) Love, J. C.; Estroff, L. A.; Kriebel, J. K.; Nuzzo, R. G.; Whitesides, G. M. *Chem. Rev.* **2005**, *105*, 1103−1169.

(26) Bain, C. D.; Whitesides, G. M. *J. Am. Chem. Soc.* **1988**, *110*, 6560−6561.

(27) Bain, C. D.; Whitesides, G. M. *J. Am. Chem. Soc.* **1989**, *111*, 7164−7175.

(28) Stranick, S. J.; Parikh, A. N.; Tao, Y. T.; Allara, D. L.; Weiss, P. S. *J. Phys. Chem.* **1994**, *98*, 7636−7646.

(29) Prado, M. C.; Neves, B. R. A. *Langmuir* **2009**, *26*, 648−654.

(30) Zschieschang, U.; Ante, F.; Schlörholz, M.; Schmidt, M.; Kern, K.; Klauk, H. *Adv. Mater.* **2010**, *22*, 4489−4493.

(31) Jedaa, A.; Salinas, M.; Jaeger, C. M.; Clark, T.; Ebel, A.; Hirsch, A.; Halik, M. *Appl. Phys. Lett.* **2012**, *100*, 063302.

(32) Rumpel, A.; Novak, M.; Walter, J.; Braunschweig, B.; Halik, M.; Peukert, W. *Langmuir* **2011**, *27*, 15016−15023.

(33) Dewar, M. J. S.; Zoebisch, E. G.; Healy, E. F.; Stewart, J. J. P. *J. Am. Chem. Soc.* **1985**, *107*, 3902−3909.

(34) Thiel, W.; Voityuk, A. *Theor. Chim. Acta* **1992**, *81*, 391−404.

(35) Winget, P.; Horn, A. H.; Selçuki, C.; Martin, B.; Clark, T. *J. Mol. Model.* **2003**, *9*, 408−414.

(36) Parr, R. G.; Yang, W. *Density Functional Theory in Atoms and Molecules*; Oxford University Press: New York, 1989.

(37) Novak, M.; Jaeger, C. M.; Rumpel, A.; Kropp, H.; Peukert, W.; Clark, T.; Halik, M. *Org. Electron.* **2010**, *11*, 1476−1482.

(38) Sun, J.; Stirner, T.; Hagston, W. E.; Leyland, A.; Matthews, A. *J. Cryst. Growth* **2006**, *290*, 235−240.

(39) Wang, J.; Wolf, R. M.; Caldwell, J. W.; Kollman, P. A.; Case, D. A. *J. Comput. Chem.* **2004**, *25*, 1157−1174.

(40) Todorov, I. T.; Smith, W.; Trachenko, K.; Dove, M. T. *J. Mater. Chem.* **2006**, *16*, 1911−1918.

(41) Darden, T.; York, D.; Pedersen, L. *J. Chem. Phys.* **1993**, *98*, 10089−10092.

(42) Beierlein, F. R.; Othersen, O. G.; Lanig, H.; Schneider, S.; Clark, T. *J. Am. Chem. Soc.* **2006**, *128*, 5142−5152.

(43) Hennemann, M.; Clark, T. Universität Erlangen-Nürnberg and Cepos InSilico Ltd., 2013; (http://www.ceposinsilico.de/products/empire.htm), accessed March 5th, 2013.

(44) Lenz, T.; Schmaltz, T.; Novak, M.; Halik, M. *Langmuir* **2012**, *28*, 13900−13904.

(45) Salinas, M.; Jäger, C. M.; Amin, A. Y.; Dral, P. O.; Meyer-Friedrichsen, T.; Hirsch, A.; Clark, T.; Halik, M. *J. Am. Chem. Soc.* **2012**, *134*, 12648−12652.

(46) Parratt, L. G. *Phys. Rev.* **1954**, *95*, 359−369.